

Provided for non-commercial research and educational use only.
Not for reproduction or distribution or commercial use.



This article was originally published in a journal published by Elsevier, and the attached copy is provided by Elsevier for the author's benefit and for the benefit of the author's institution, for non-commercial research and educational use including without limitation use in instruction at your institution, sending it to specific colleagues that you know, and providing a copy to your institution's administrator.

All other uses, reproduction and distribution, including without limitation commercial reprints, selling or licensing copies or access, or posting on open internet sites, your personal or institution's website or repository, are prohibited. For exceptions, permission may be sought for such use through Elsevier's permissions site at:

<http://www.elsevier.com/locate/permissionusematerial>

Numerical simulation of 3-D wing flutter with fully coupled fluid–structural interaction

Xiangying Chen ^{a,*}, Ge-Cheng Zha ^a, Ming-Ta Yang ^b

^a Department of Mechanical and Aerospace Engineering, University of Miami, Coral Gables, FL 33124, USA

^b Discipline Engineering-Structures, Pratt and Whitney, 400 Main Street, MIS 163-07, East Hartford, CT 06108, USA

Received 21 March 2006; received in revised form 18 July 2006; accepted 17 August 2006

Available online 26 January 2007

Abstract

A numerical methodology coupling Navier–Stokes equations and structural modal equations for predicting 3-D transonic wing flutter is developed in this paper. A dual-time step implicit unfactored Gauss–Seidel iteration with the Roe scheme is employed for the flow solver. A modal approach is used for the structural response. The flow and structural solvers are fully coupled via successive iterations within each physical time step. The mesh-deformation strategy is described. The accuracy of the modal approach is validated with ANSYS. The results indicate that the first five modes are sufficient to accurately model the wing-structure response for the studied case of this paper. The computed flutter boundary of AGARD wing 445.6 at free stream Mach numbers ranging from 0.499 to 1.141 agrees well with the experiment.

© 2006 Elsevier Ltd. All rights reserved.

1. Introduction

Reliable and efficient flutter analysis of airplane wings or aircraft-engine turbomachinery blades is a critical issue in determining the reliability of aircraft. Flutter occurs as a result of the fluid–structural interaction and is usually associated with complicated phenomena such as the shock wave/boundary layer interaction, flow separation, non-linear limit cycle oscillations, etc. Flutter predictions using a three-dimensional Navier–Stokes with fully coupled iteration are very challenging due to the perplexing physical phenomena and the large amount of computation work. In the present paper, an effort has been made to develop a methodology for high fidelity prediction of aircraft flutter.

There are generally two types of methods used to calculate the fluid–structure interaction problems in the time

domain: the fluid and structure governing equations are loosely coupled or fully coupled. The loosely coupled model means that the structural response lags behind the flow field solution. This type of method may be limited to first-order accuracy in time regardless of the temporal accuracy of the individual solvers [1]. In the fully coupled model, the flow field and structure always respond simultaneously by exchanging the aerodynamic forcing and structural displacement within each iteration. Logically, only the fully coupled model is rigorous in the physical sense because, in reality, the structural displacement responds instantly to the forces acted by the fluid.

Among the researchers in the area of 3-D time-marching aeroelastic analysis based on Euler/Navier–Stokes approaches, Lee-Rausch and Batina [2,3] used a three-factor, implicit, upwind-biased Euler/Navier–Stokes approach coupled with a lagged structure solver. Morton, Melville and Gordnier et al. developed an implicit fully coupled fluid-structure interaction model, which used the Beam-Warming implicit approximate factorization scheme for the flow solver coupled with a modal structural solver [4,5,1,6]. Liu et al. developed a fully coupled method using

* Corresponding author. Tel.: +1 305 284 2571; fax: +1 305 284 2580.
E-mail address: gzha@miami.edu (X. Chen).

Jameson's explicit scheme with a multigrid approach utilizing the Euler equations and a modal structural model [7]. Doi and Alonso [8] coupled an explicit Runge–Kutta multigrid RANS flow solver with a FEM structure solver to predict the aeroelastic responses of a NASA Rotor 67 blade.

Chen et al. [9,10] have recently developed a fully coupled methodology between fluid and structure for 2-D flow-induced vibrations. In their method, the Roe scheme is extended to the moving grid system. The unsteady solutions march in time by using a dual-time stepping implicit unfactored Gauss-Seidel iteration. The unsteady Navier–Stokes equations and the structural equations are fully coupled implicitly via successive iteration within each physical time step.

In present study, the method developed by Chen et al. [9,10] is extended to 3-D transonic flutter prediction of a flexible wing. The structural response is calculated by the efficient modal approach. Compared with the different methods aforementioned for 3-D aeroelastic analysis, the methodology of this paper has the following advantages:

- (1) The unfactored Gauss-Seidel iteration is unconditionally stable and allows larger pseudo or physical time steps than an explicit method. It avoids the factorization error introduced by those implicit approximate factorization methods, such as those used in [2,4,5,1,6]. Even though the factorization error diminishes within each physical time step, the factorization error can limit the numerical stability. The linear stability analysis shows that an approximate factorized method is not stable for 3-D computation even though it is stable for 2-D computation.
- (2) Unlike the central differencing schemes used in [4,5,1,6,7], the Roe scheme has inherent low dissipation and does not need additional artificial dissipation, which may need to be calibrated case by case. The adjusted numerical dissipation may significantly affect the flow damping of the structural response.
- (3) As mentioned previously, the fully coupled approach is a rigorous approach to reflect the instantaneous interaction between the flow and structure and is more accurate than the loosely coupled methods such as those used in [2,3,8].

The objective of this paper is to develop a methodology for 3-D transonic wing-flutter prediction with fully coupled fluid-structure interaction. The modal approach structure solver is used for the structural response in the computation. The flutter boundary of AGARD Wing 445.6 is predicted for free stream Mach numbers ranging from 0.499 to 1.141. In general, the computed results show good agreement with the experiment and indicate that the present methodology is robust and accurate for realistic aeroelastic analysis.

2. CFD aerodynamic model

2.1. Flow governing equations

The governing equations for the flow field computation are the Reynolds-Averaged Navier–Stokes equations (RANS) with Favre mass average which can be transformed to the generalized coordinates (ξ, η, ζ) and expressed as

$$\frac{\partial \mathbf{Q}'}{\partial t} + \frac{\partial \mathbf{E}'}{\partial \xi} + \frac{\partial \mathbf{F}'}{\partial \eta} + \frac{\partial \mathbf{G}'}{\partial \zeta} = \frac{1}{Re} \left(\frac{\partial \mathbf{E}'_v}{\partial \xi} + \frac{\partial \mathbf{F}'_v}{\partial \eta} + \frac{\partial \mathbf{G}'_v}{\partial \zeta} \right) \quad (1)$$

where Re is the Reynolds number and

$$\mathbf{Q}' = \frac{\mathbf{Q}}{J} \quad (2)$$

$$\mathbf{E}' = \frac{1}{J} (\xi_t \mathbf{Q} + \xi_x \mathbf{E} + \xi_y \mathbf{F} + \xi_z \mathbf{G}) = \frac{1}{J} (\xi_t \mathbf{Q} + \mathbf{E}'') \quad (3)$$

$$\mathbf{F}' = \frac{1}{J} (\eta_t \mathbf{Q} + \eta_x \mathbf{E} + \eta_y \mathbf{F} + \eta_z \mathbf{G}) = \frac{1}{J} (\eta_t \mathbf{Q} + \mathbf{F}'') \quad (4)$$

$$\mathbf{G}' = \frac{1}{J} (\zeta_t \mathbf{Q} + \zeta_x \mathbf{E} + \zeta_y \mathbf{F} + \zeta_z \mathbf{G}) = \frac{1}{J} (\zeta_t \mathbf{Q} + \mathbf{G}'') \quad (5)$$

$$\mathbf{E}'_v = \frac{1}{J} (\xi_x \mathbf{E}_v + \xi_y \mathbf{F}_v + \xi_z \mathbf{G}_v) \quad (6)$$

$$\mathbf{F}'_v = \frac{1}{J} (\eta_x \mathbf{E}_v + \eta_y \mathbf{F}_v + \eta_z \mathbf{G}_v) \quad (7)$$

$$\mathbf{G}'_v = \frac{1}{J} (\zeta_x \mathbf{E}_v + \zeta_y \mathbf{F}_v + \zeta_z \mathbf{G}_v) \quad (8)$$

where the geometry metrics are defined as

$$\begin{aligned} \xi_x &= J(y_\eta z_\zeta - y_\zeta z_\eta), & \xi_y &= J(x_\zeta z_\eta - x_\eta z_\zeta), \\ \xi_z &= J(x_\eta y_\zeta - x_\zeta y_\eta), & \eta_x &= J(y_\zeta z_\xi - y_\xi z_\zeta), \\ \eta_y &= J(x_\zeta z_\xi - x_\xi z_\zeta), & \eta_z &= J(x_\xi y_\zeta - x_\zeta y_\xi), \\ \zeta_x &= J(y_\zeta z_\eta - y_\eta z_\zeta), & \zeta_y &= J(x_\eta z_\xi - x_\xi z_\eta), \\ \zeta_z &= J(x_\xi y_\eta - x_\eta y_\xi), & \zeta_t &= -(x_t \xi_x + y_t \xi_y + z_t \xi_z), \\ \eta_t &= -(x_t \eta_x + y_t \eta_y + z_t \eta_z), & \zeta_t &= -(x_t \zeta_x + y_t \zeta_y + z_t \zeta_z) \end{aligned}$$

The variable vector \mathbf{Q} , and inviscid flux vectors \mathbf{E} , \mathbf{F} , and \mathbf{G} are:

$$\mathbf{Q} = \begin{pmatrix} \bar{\rho} \\ \bar{\rho} \tilde{u} \\ \bar{\rho} \tilde{v} \\ \bar{\rho} \tilde{w} \\ \bar{\rho} \tilde{e} \end{pmatrix}, \quad \mathbf{E} = \begin{pmatrix} \bar{\rho} \tilde{u} \\ \bar{\rho} \tilde{u} \tilde{u} + \tilde{p} \\ \bar{\rho} \tilde{u} \tilde{v} \\ \bar{\rho} \tilde{u} \tilde{w} \\ (\bar{\rho} \tilde{e} + \tilde{p}) \tilde{u} \end{pmatrix},$$

$$\mathbf{F} = \begin{pmatrix} \bar{\rho} \tilde{v} \\ \bar{\rho} \tilde{u} \tilde{v} \\ \bar{\rho} \tilde{v} \tilde{v} + \tilde{p} \\ \bar{\rho} \tilde{v} \tilde{w} \\ (\bar{\rho} \tilde{e} + \tilde{p}) \tilde{v} \end{pmatrix}, \quad \mathbf{G} = \begin{pmatrix} \bar{\rho} \tilde{w} \\ \bar{\rho} \tilde{u} \tilde{w} \\ \bar{\rho} \tilde{v} \tilde{w} \\ \bar{\rho} \tilde{w} \tilde{w} + \tilde{p} \\ (\bar{\rho} \tilde{e} + \tilde{p}) \tilde{w} \end{pmatrix}$$

The \mathbf{E}'' , \mathbf{F}'' , and \mathbf{G}'' are the inviscid fluxes at the stationary grid system and can be expressed as

$$\mathbf{E}'' = \xi_x \mathbf{E} + \xi_y \mathbf{F} + \xi_z \mathbf{G},$$

$$\mathbf{F}'' = \eta_x \mathbf{E} + \eta_y \mathbf{F} + \eta_z \mathbf{G},$$

$$\mathbf{G}'' = \zeta_x \mathbf{E} + \zeta_y \mathbf{F} + \zeta_z \mathbf{G}$$

and the viscous flux vectors are given by

$$\mathbf{E}_v = \begin{pmatrix} 0 \\ \bar{\tau}_{xx} - \overline{\rho u'' u''} \\ \bar{\tau}_{xy} - \overline{\rho u'' v''} \\ \bar{\tau}_{xz} - \overline{\rho u'' w''} \\ Q_x \end{pmatrix}, \quad \mathbf{F}_v = \begin{pmatrix} 0 \\ \bar{\tau}_{yx} - \overline{\rho v'' u''} \\ \bar{\tau}_{yy} - \overline{\rho v'' v''} \\ \bar{\tau}_{yz} - \overline{\rho v'' w''} \\ Q_y \end{pmatrix},$$

$$\mathbf{G}_v = \begin{pmatrix} 0 \\ \bar{\tau}_{zx} - \overline{\rho w'' u''} \\ \bar{\tau}_{zy} - \overline{\rho w'' v''} \\ \bar{\tau}_{zz} - \overline{\rho w'' w''} \\ Q_z \end{pmatrix}$$

In above equations, ρ is the density, u , v , and w are the Cartesian velocity components in x , y and z directions, respectively, p is the static pressure, and e is the total energy per unit mass. The overbar denotes the Reynolds-averaged quantity, tilde and double-prime denote the Favre mean and Favre fluctuating part of the turbulent motion respectively. All the flow variable in above equations are normalized by the freestream quantities and a reference length L .

Let subscript 1, 2 and 3 represent the coordinates, x , y , and z , and use Einstein summation convention, the shear-stress and Q_x , Q_y , Q_z terms in non-dimensional forms can be expressed in tensor form as

$$\bar{\tau}_{ij} = -\frac{2}{3} \tilde{\mu} \frac{\partial \tilde{u}_k}{\partial x_k} \delta_{ij} + \tilde{\mu} \left(\frac{\partial \tilde{u}_i}{\partial x_j} + \frac{\partial \tilde{u}_j}{\partial x_i} \right) \quad (9)$$

$$Q_i = \tilde{u}_j (\bar{\tau}_{ij} - \overline{\rho u'' u''}) - (\bar{q}_i + C_p \rho \overline{T'' u''_i}) \quad (10)$$

where the mean molecular heat flux is

$$\bar{q}_i = -\frac{\tilde{\mu}}{(\gamma - 1) Pr} \frac{\partial a^2}{\partial x_i} \quad (11)$$

The molecular viscosity $\tilde{\mu} = \tilde{\mu}(\tilde{T})$ is determined by Sutherland law, and $a = \sqrt{\gamma R T_\infty}$ is the speed of sound. The equation of state closes the system

$$\bar{\rho} \tilde{e} = \frac{\tilde{p}}{(\gamma - 1)} + \frac{1}{2} \bar{\rho} (\tilde{u}^2 + \tilde{v}^2 + \tilde{w}^2) + k \quad (12)$$

where γ is the ratio of specific heats, k is the Favre mass-averaged turbulence kinetic energy. The turbulent shear stresses and heat flux appeared in above equations are calculated by Baldwin–Lomax model [11]. The viscosity is composed of $\mu + \mu_t$, where μ is the molecular viscosity and μ_t is the turbulent viscosity determined by Baldwin Lomax model. For a laminar flow, the μ_t is set to be zero.

2.2. Time marching scheme

The time dependent governing equation (1) is solved using the control volume method with the concept of dual

time stepping suggested by Jameson [12]. A pseudo temporal term $\frac{\partial \mathbf{Q}}{\partial \tau}$ is added to the governing Eq. (1). This term vanishes at the end of each physical time step, and has no influence on the accuracy of the solution. However, instead of using the explicit scheme as given by Jameson in [12], an implicit pseudo time marching scheme using line Gauss-Seidel line iteration is employed to achieve high convergence rate. The physical temporal term is discretized implicitly using a three point, backward differencing as the following:

$$\frac{\partial \mathbf{Q}}{\partial t} = \frac{3Q^{n+1} - 4Q^n + Q^{n-1}}{2\Delta t} \quad (13)$$

where n is the time level index. The pseudo temporal term is discretized with the first order Euler scheme. Let m stand for the iteration index within a physical time step, then the semi-discretized governing equation (1) can be expressed as

$$\left[\left(\frac{1}{\Delta \tau} + \frac{1.5}{\Delta t} \right) I - \left(\frac{\partial R}{\partial Q} \right)^{n+1, m} \right] \delta Q^{n+1, m+1} = R^{n+1, m} - \frac{3Q^{n+1, m} - 4Q^n + Q^{n-1}}{2\Delta t} \quad (14)$$

where the $\Delta \tau$ is the pseudo time step, R is the net flux going through the control volume,

$$R = -\frac{1}{V} \int_s [(F - F_v)\mathbf{i} + (G - G_v)\mathbf{j} + (H - H_v)\mathbf{k}] \cdot d\mathbf{s} \quad (15)$$

where V is the volume of the control volume, \mathbf{s} is the control volume surface area vector.

Since the O-mesh is used, the line tri-diagonal block matrix solver is along the ξ direction, which is around the airfoil on a 2D plane. Two alternating direction line sweeps are used in each pseudo time step with one sweep from minimum η , ζ index to maximum index, and the other from maximum index to minimum index. The alternative sweep directions are beneficial for the information propagation to reach a high convergence rate. Within each physical time step, the solution marches in pseudo time until converged. The method is unconditionally stable and can reach a very large pseudo time step since no factorization error is introduced.

2.3. Roe's Riemann solver on moving grid system

An accurate Riemann solver is necessary to resolve the shock wave and wall boundary layer in the flow field. The Roe scheme [13] is selected and implemented in the code to evaluate the inviscid fluxes with the 3rd order MUSCL type differencing [14]. In the present study, the original Roe scheme is extended to a moving-grid system as the following, for example, in ξ direction:

$$\mathbf{E}'_{i+\frac{1}{2}} = \frac{1}{2J} [\mathbf{E}''(\mathbf{Q}_L) + \mathbf{E}''(\mathbf{Q}_R) + \mathbf{Q}_L \xi_{iL} + \mathbf{Q}_R \xi_{iR} - |\tilde{\mathbf{A}}|(\mathbf{Q}_R - \mathbf{Q}_L)]_{i+\frac{1}{2}} \quad (16)$$

where \mathbf{Q}_L and \mathbf{Q}_R are the reconstructed variables to the left and right sides of the cell face, ξ_{iL} and ξ_{iR} are the reconstructed grid velocity components in ξ -direction to the left and right sides of the cell interface $i + \frac{1}{2}$, \mathbf{A} is the Jacobian matrix, $\mathbf{A} = \frac{\partial \mathbf{E}'}{\partial \mathbf{Q}}$ and it takes the form $\mathbf{A} = \mathbf{T}\mathbf{\Lambda}\mathbf{T}^{-1}$, where \mathbf{T} is the right eigenvector matrix of \mathbf{A} , $\mathbf{\Lambda}$ is the eigenvalue matrix of \mathbf{A} , and

$$\tilde{\mathbf{A}} = \tilde{\mathbf{T}}\tilde{\mathbf{\Lambda}}\tilde{\mathbf{T}}^{-1} \quad (17)$$

where $\tilde{\mathbf{A}}$ is the eigenvalue matrix on a moving-grid system with the eigenvalues of

$$(\tilde{U} + \tilde{C}, \tilde{U} - \tilde{C}, \tilde{U}, \tilde{U}, \tilde{U}) \quad (18)$$

where \tilde{U} is the contravariant velocity in the ξ -direction on the moving grid,

$$\tilde{U} = \tilde{\xi}_t + \xi_x \tilde{u} + \xi_y \tilde{v} + \xi_z \tilde{w} \quad (19)$$

\tilde{C} is the speed of sound corresponding to the contravariant velocity:

$$\tilde{C} = \tilde{c} \sqrt{\xi_x^2 + \xi_y^2 + \xi_z^2} \quad (20)$$

where $c = \sqrt{\gamma RT}$ is the physical speed of sound. The \sim stands for the Roe-averaged quantities. For example,

$$\tilde{\xi}_t = (\xi_{iL} + \xi_{iR} \sqrt{\rho_R/\rho_L}) / (1 + \sqrt{\rho_R/\rho_L}) \quad (21)$$

It can be proved that the eigenvector matrix \mathbf{T} has exactly the same form as the one without a moving grid. The only difference between the moving-grid and the stationary-grid systems is that, for the moving-grid system, the contravariant velocity in the eigenvalues contains the grid velocity as given in Eq. (19). It is hence straightforward to extend the code from a stationary-grid system to the moving-grid system using the Roe scheme without a major change.

The grid velocity is evaluated at the center of each cell and is determined by the averaged value that counts the movement of the eight vertexes if hexahedral control volumes are used. The grid velocity is reconstructed with 3rd-order MUSCL differencing.

2.4. Boundary conditions

The boundary conditions for the computation of wing flutter are as follows:

- (1) Upstream boundary conditions: The outer boundary is divided into upstream and downstream boundaries according to whether the direction of its segment is toward or backward to the incoming-flow direction. On the upstream boundary, it is assumed that the streamwise velocity u is uniform, the transverse velocity $v = 0$, and the spanwise velocity $w = 0$. Other primitive variables are specified according to the free-stream condition except the pressure which is extrapolated from the interior.

- (2) Downstream boundary conditions: All the flow quantities are extrapolated from the interior except the static pressure which is set to equal its freestream value.
- (3) Solid wall boundary conditions: At a moving-boundary surface, the no-slip condition is enforced by extrapolating the velocity between the phantom and interior cells,

$$u_0 = 2\dot{x}_b - u_1, \quad v_0 = 2\dot{y}_b - v_1, \quad w_0 = 2\dot{z}_b - w_1 \quad (22)$$

where u_0, v_0 and w_0 denote the velocity at the phantom cell, u_1, v_1 and w_1 denote the velocity at the first interior cell close to the boundary, and u_b, v_b and w_b are the velocity components on the moving boundary.

If the wall surface is in η direction, the other two conditions to be imposed on the solid wall are the adiabatic wall condition and the inviscid normal momentum equation [4] as follows:

$$\frac{\partial T}{\partial \eta} = 0, \quad \frac{\partial p}{\partial \eta} = - \left(\frac{\rho}{\eta_x^2 + \eta_y^2 + \eta_z^2} \right) (\eta_x \ddot{x}_b + \eta_y \ddot{y}_b + \eta_z \ddot{z}_b) \quad (23)$$

2.5. Moving/deforming grid systems

In the fully coupled computation, the remeshing is performed in each iteration. Therefore, a CPU time-efficient algebraic grid-deformation method is employed in the computation instead of the commonly used grid-generation method in which the Poisson equation is solved for grid points. For clarity, the remeshing procedure for 2D cases is sketched in Fig. 1. This grid deformation procedure is designed in such a way that the far-field boundary ($j = jlp$) is held fixed, and the grids on the wing surface ($j = 1$) move and deform following the instantaneous

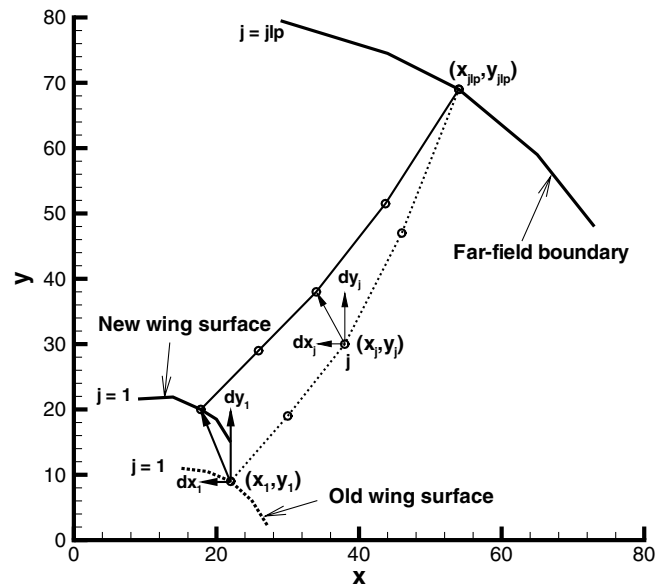


Fig. 1. A sketch of the mesh deformation.

motion of the wing structure. After the new wing surface is determined, two components of the displacement vector at a wing surface node dx_1 and dy_1 can be calculated accordingly. First, the length of each segment along the old mesh line is estimated as

$$s_j = s_{j-1} + \sqrt{(x_j - x_{j-1})^2 + (y_j - y_{j-1})^2} \quad (j = 2, \dots, jlp) \quad (24)$$

where $s_1 = 0$ and the displacement vectors at wing surface node (dx_1, dy_1) and at the far-field boundary (dx_{jlp}, dy_{jlp}) are known. Then the grid node points between the wing surface and the far-field boundary can be obtained by using following linear interpolation:

$$dx_j = \frac{dx_{jlp} - dx_1}{s_{jlp} - s_1} s_j + \frac{dx_1 s_{jlp} - dx_{jlp} s_1}{s_{jlp} - s_1} \quad (25)$$

$$dy_j = \frac{dy_{jlp} - dy_1}{s_{jlp} - s_1} s_j + \frac{dy_1 s_{jlp} - dy_{jlp} s_1}{s_{jlp} - s_1} \quad (26)$$

This simple remeshing strategy is proved to be robust for all the cases investigated in the present study. By monitoring the accuracy criterion y^+ , it is shown that the method can maintain the initial grid quality and keep almost the same mesh distribution around the wing surface.

For a 3-D case, Eq. (24) becomes

$$s_j = s_{j-1} + \sqrt{(x_j - x_{j-1})^2 + (y_j - y_{j-1})^2 + (z_j - z_{j-1})^2} \quad (j = 2, \dots, jlp) \quad (27)$$

and one more equation is added to determine the z component of displacement vector:

$$dz_j = \frac{dz_{jlp} - dz_1}{s_{jlp} - s_1} s_j + \frac{dz_1 s_{jlp} - dz_{jlp} s_1}{s_{jlp} - s_1} \quad (28)$$

2.6. Geometric conservation law

It was pointed out by Thomas et al. [15] that due to the mixed temporal and spatial derivatives after discretization, an additional term appears, which theoretically equals to zero but numerically still remains. Consequently numerical errors could be introduced into the discretized form of the equations of the flow motion if this term is neglected. In order to reduce or avoid this error, the geometric conservation law needs to be enforced. In other words, the following additional term should be added to the right-hand side of the equations as a source term:

$$\mathbf{S} = \mathbf{Q} \left[\frac{\partial J^{-1}}{\partial t} + \left(\frac{\xi_t}{J} \right)_\xi + \left(\frac{\eta_t}{J} \right)_\eta + \left(\frac{\zeta_t}{J} \right)_\zeta \right] \quad (29)$$

To implement this option in the flow solver, the source term is then linearized such that

$$\mathbf{S}^{n+1} = \mathbf{S}^n + \frac{\partial \mathbf{S}}{\partial \mathbf{Q}} \Delta \mathbf{Q}^{n+1} \quad (30)$$

As has been observed, the overall performance of this numerical supplement is beneficial with very little extra CPU-time cost.

3. Structural model of a three dimensional wing

3.1. Modal approach

The governing equation of a solid structure's motion can be written as

$$\mathbf{M} \frac{d^2 \mathbf{u}}{dt^2} + \mathbf{C} \frac{d\mathbf{u}}{dt} + \mathbf{K} \mathbf{u} = \mathbf{f} \quad (31)$$

where \mathbf{M} , \mathbf{C} and \mathbf{K} are the mass, damping, and stiffness matrices of the solid structure respectively, \mathbf{u} is the displacement vector and \mathbf{f} is the force exerted on the surface node points of the solid, both can be expressed as

$$\mathbf{u} = \begin{pmatrix} \mathbf{u}_1 \\ \vdots \\ \mathbf{u}_i \\ \vdots \\ \mathbf{u}_N \end{pmatrix}, \quad \mathbf{f} = \begin{pmatrix} \mathbf{f}_1 \\ \vdots \\ \mathbf{f}_i \\ \vdots \\ \mathbf{f}_N \end{pmatrix}$$

where N is the total number of node points of the structural model, \mathbf{u}_i and \mathbf{f}_i are vectors with three components in x, y, z directions:

$$\mathbf{u}_i = \begin{pmatrix} \mathbf{u}_{ix} \\ \mathbf{u}_{iy} \\ \mathbf{u}_{iz} \end{pmatrix}, \quad \mathbf{f}_i = \begin{pmatrix} \mathbf{f}_{ix} \\ \mathbf{f}_{iy} \\ \mathbf{f}_{iz} \end{pmatrix}$$

\mathbf{f}_i is dynamic force exerted on the surface of the solid body. In a modal approach, the modal decomposition of the structure motion can be expressed as the following:

$$\mathbf{K} \Phi = \mathbf{M} \Phi \Lambda \quad (32)$$

or

$$\mathbf{K} \phi_j = \lambda_j \mathbf{M} \phi_j \quad (33)$$

where Λ is the eigenvalue matrix, $\Lambda = \text{diag}[\lambda_1, \dots, \lambda_j, \dots, \lambda_{3N}]$, $\lambda_j = \omega_j^2$, where ω_j is the natural frequency of j th mode, and the mode shape matrix $\Phi = [\phi_1, \dots, \phi_j, \dots, \phi_{3N}]$.

Eq. (33) can be solved by using a finite element solver (e.g. ANSYS) to obtain its finite number of mode shapes ϕ_j . The first five mode shapes will be used in this paper to calculate the displacement of the structure such that

$$\mathbf{u}(t) = \sum_j a_j(t) \phi_j = \Phi \mathbf{a} \quad (34)$$

where $\mathbf{a} = [a_1, a_2, a_3, a_4, a_5]^T$. Substituting Eq. (34) to Eq. (31) yields

$$\mathbf{M} \Phi \frac{d^2 \mathbf{a}}{dt^2} + \mathbf{C} \Phi \frac{d\mathbf{a}}{dt} + \mathbf{K} \Phi \mathbf{a} = \mathbf{f} \quad (35)$$

Multiplying Eq. (35) by Φ^T and re-writing it as

$$\hat{\mathbf{M}} \frac{d^2 \mathbf{a}}{dt^2} + \hat{\mathbf{C}} \frac{d\mathbf{a}}{dt} + \hat{\mathbf{K}} \mathbf{a} = \mathbf{P} \quad (36)$$

where $\mathbf{P} = [P_1, P_2, \dots, P_j, \dots, P_N]^T$, the modal force of j th mode is $P_j = \phi_j^T \mathbf{f}$, the modal mass matrix is defined as

$$\hat{\mathbf{M}} = \Phi^T \mathbf{M} \Phi = \text{diag}(m_1, \dots, m_j, \dots, m_{3N}) \quad (37)$$

where m_j is the modal mass of j th mode, and the modal damping matrix is defined as

$$\hat{\mathbf{C}} = \Phi^T \mathbf{C} \Phi = \text{diag}(c_1, \dots, c_j, \dots, c_{3N}) \quad (38)$$

where c_j is the modal damping of j th mode, and the modal stiffness matrix is defined as

$$\hat{\mathbf{K}} = \Phi^T \mathbf{K} \Phi = \text{diag}(k_1, \dots, k_j, \dots, k_{3N}) \quad (39)$$

where k_j is the modal stiffness of j th mode. Eq. (36) implies

$$\frac{d^2 a_j}{dt^2} + 2\zeta_j \omega_j \frac{da_j}{dt} + \omega_j^2 a_j = \frac{\phi_j^T \mathbf{f}}{m_j} \quad (40)$$

where ζ_j is modal damping ratio. Eq. (40) is the modal equation of structure motion, and is solved numerically within each iteration. By carefully choosing reference quantities, the normalized equation may be expressed as

$$\frac{d^2 a_j}{dt^{*2}} + 2\zeta_j \left(\frac{\omega_j}{\omega_x}\right) \frac{da_j}{dt^*} + \left(\frac{\omega_j}{\omega_x}\right)^2 a_j = \phi_j^{*T} \mathbf{f}^* V^* \left(\frac{b_s}{L}\right)^2 \frac{\bar{m}}{v^*} \quad (41)$$

where the dimensionless quantities are denoted by an asterisk, ω_x is the natural frequency in pitch, b_s is the streamwise semichord measured at the wing's root, L is the reference length, \bar{m} is the measured wing-panel mass, v^* is the volume of a conical frustum having the streamwise root chord as its lower base diameter, the streamwise tip chord as its upper base diameter, and the panel span as its height, $V^* = \frac{U_\infty}{b_s \omega_x \sqrt{\bar{\mu}}}$, and U_∞ is the freestream velocity.

Then the equations are transformed to a state form and expressed as

$$[\mathbf{M}] \frac{\partial \{\mathbf{S}\}}{\partial t} + [\mathbf{K}] \{\mathbf{S}\} = \mathbf{q} \quad (42)$$

where

$$\mathbf{S} = \begin{pmatrix} a_j \\ \dot{a}_j \end{pmatrix}, \quad \mathbf{M} = [I], \quad \mathbf{K} = \begin{pmatrix} 0 & -1 \\ \left(\frac{\omega_j}{\omega_x}\right)^2 & 2\zeta_j \left(\frac{\omega_j}{\omega_x}\right) \end{pmatrix},$$

$$\mathbf{q} = \begin{pmatrix} 0 \\ \phi_j^{*T} \mathbf{f}^* V^* \left(\frac{b_s}{L}\right)^2 \frac{\bar{m}}{v^*} \end{pmatrix}$$

To couple the structural equations with the equations of flow motion and solve them implicitly in each physical time step, the above equations are discretized and integrated in a manner consistent with Eq. (14) to yield

$$\begin{aligned} & \left(\frac{1}{\Delta\tau} \mathbf{I} + \frac{1.5}{\Delta t} \mathbf{M} + \mathbf{K} \right) \delta S^{n+1,m+1} \\ & = -\mathbf{M} \frac{3S^{n+1,m} - 4S^n + S^{n-1}}{2\Delta t} - \mathbf{K} S^{n+1,m} + \mathbf{q}^{n+1,m+1} \end{aligned} \quad (43)$$

where n is the physical time level index while m stands for the pseudo time index. The detailed coupling procedure between the fluid and structural systems is given in the following section.

4. Fully coupled fluid-structural interaction procedure

To rigorously simulate fluid-structural interactions, the equations of flow motion and structural response need to be solved simultaneously within each iteration in a fully coupled numerical model. The calculation based on fully coupled iteration is CPU expensive, especially for three dimensional applications. The modal approach can save CPU time significantly by solving the modal displacement equations, Eq. (40), instead of the original structural equations, Eq. (33), which is usually solved by using a finite element method. In the modal approach, the structural mode shapes can be pre-determined by using a separate finite element structural solver. Once the several mode shapes of interest are obtained, the physical displacements can be calculated just by solving those simplified linear equations, i.e., Eqs. (40) and (34). In present study, the first five mode shapes provided in Ref. [16] are used to model the wing structure. These pre-calculated mode shapes are obtained on a fixed structural grid system and are transformed to the CFD grid system by using a 3rd order polynomial

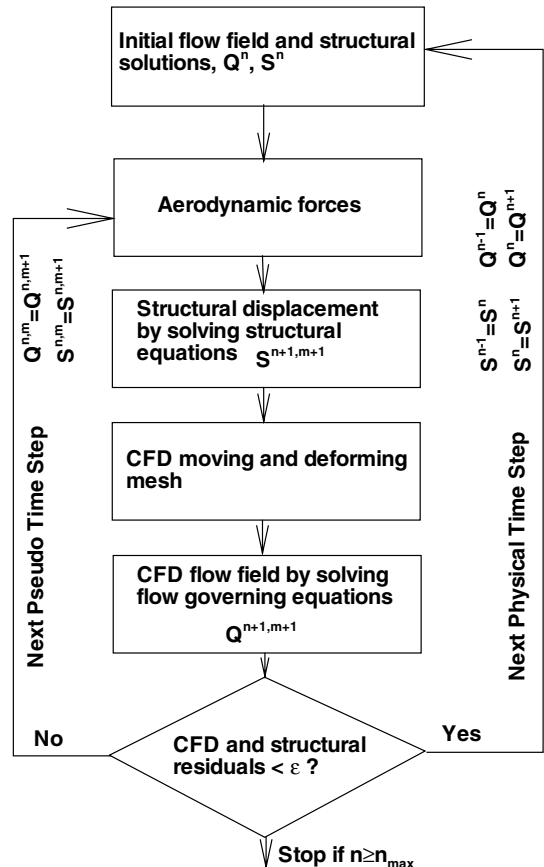


Fig. 2. Fully coupled flow-structure interaction procedure.

Table 1
Free-stream condition for ONERA M6 wing

Mach number	0.8395
Static pressure (psia)	12.2913
Temperature (R)	447.0
Angle-of-attack (deg)	0.0
Reynolds number	19.7×10^6
Aspect ratio	3.8

fitting procedure. The procedure is only performed once and then the mode shapes for the CFD grid system are stored in the code throughout the simulation.

The procedure for the fully coupled fluid-structure interaction by the modal approach is described below:

- (1) The flow solver provides dynamic forces on solid surfaces.
- (2) The fluid forces are integrated at each surface element to obtain the forcing vector \mathbf{f} .

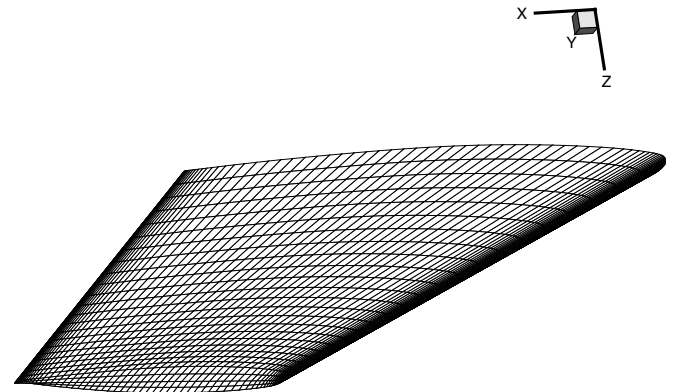


Fig. 3. The mesh on the ONERA M6 wing surface.

- (3) Eq. (40) is used to calculate the modal displacements a_j ($j = 1, 2, 3, 4, 5$) of the next pseudo time step.
- (4) Eq. (34) is used to calculate the physical displacement \mathbf{u} of the next pseudo time step.

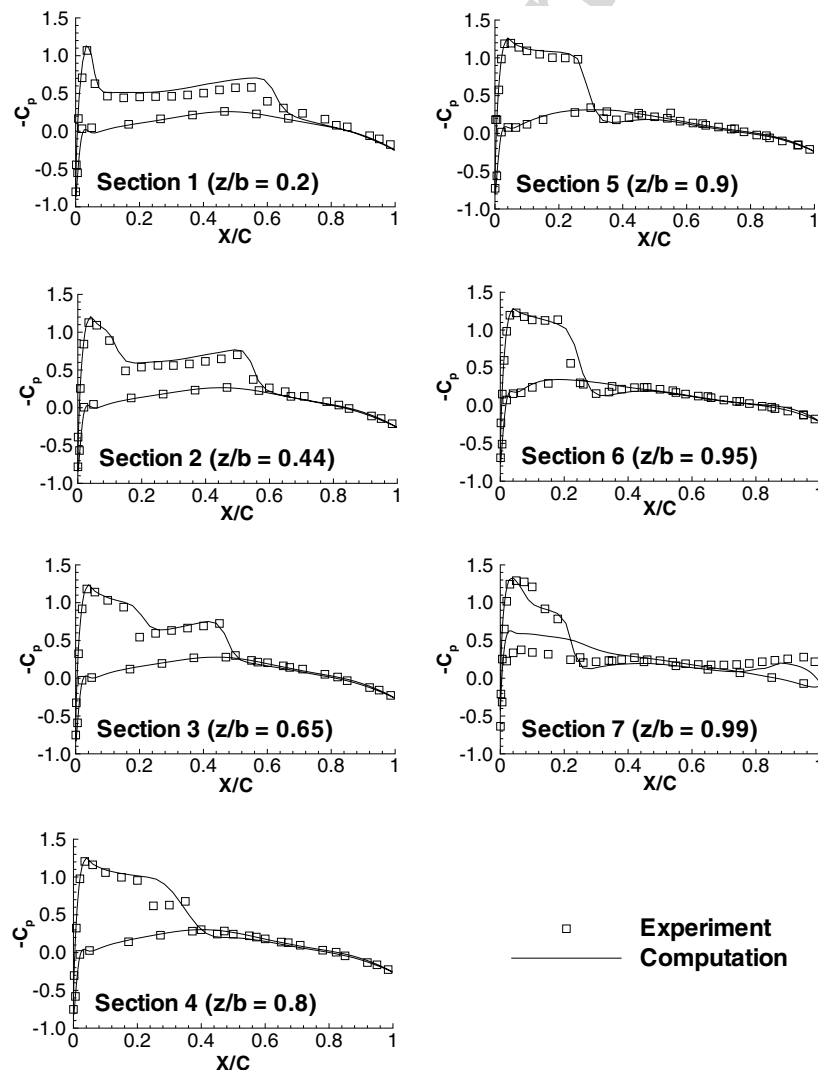


Fig. 4. Pressure coefficients on the ONERA M6 wing surface at different cross sections.

- (5) The maximum residuals of both solutions of the flow and the structural equations are checked. If the maximum residuals are greater than the prescribed convergence criteria, go back to step (1) and proceed to the next pseudo time. Otherwise the calculation of the flow field and the structural displacement within the physical time step is completed and the next new physical time step starts. The procedure is also illustrated in the flow chart given in Fig. 2.

5. Results and discussion

The result for the steady state transonic ONERA M6 wing is calculated first in order to validate the 3-D CFD solver. Then a plate wing is calculated and the results are compared with the solution of finite element solver. Finally, the flutter boundary of an AGARD wing 445.6 is calculated.

5.1. Steady state transonic ONERA M6 wing

As a validation of the three dimensional solver for a transonic wing, the steady state solution of the transonic

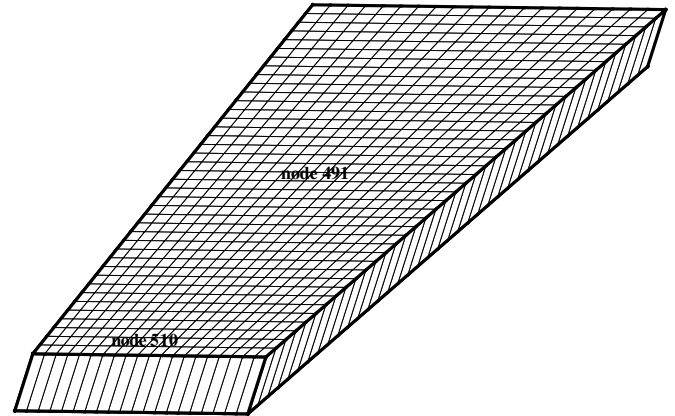
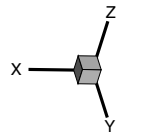


Fig. 5. Plate wing geometry.

ONERA M6 wing is calculated. The freestream conditions for this study are listed in Table 1 below.

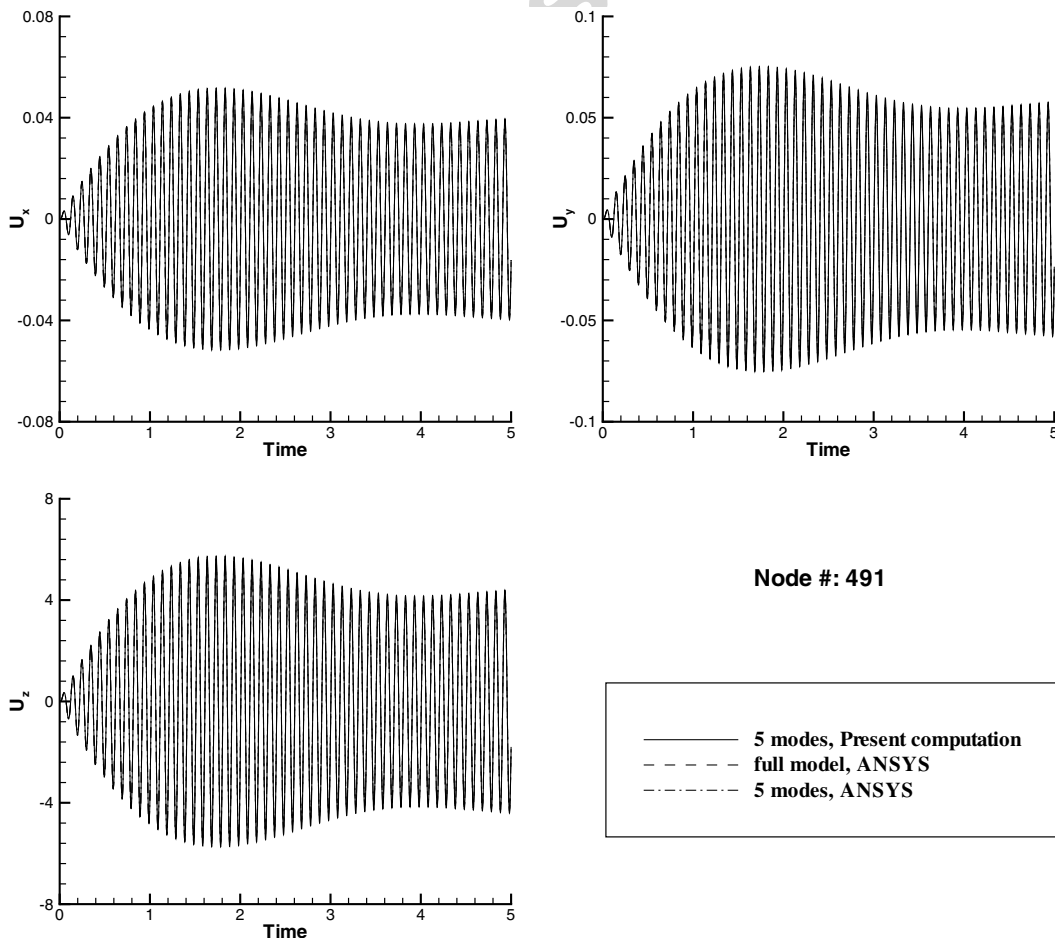


Fig. 6. Histories of the dynamic responses at node point 491.

This case is calculated using an O-type grid with the dimension of 144 (around wing) \times 60 (normal to the wing) \times 40 (spanwise). The far field boundary is located 15 chords away from the chord center of the wing. The surface mesh of the wing is depicted in Fig. 3.

The computed surface pressure distributions at various cross sections are shown in Fig. 4 with the experimental data given by Schmitt et al. [17]. The location of $z/b = 0.2$ is near the root, and $z/b = 0.99$ is at wing tip.

Overall, very good agreement is obtained between the computation and experiment for each cross-section except at the section of $z/b = 0.8$, where the double-shock pattern is not very well resolved.

5.2. Validation of structural solver

To validate the structural model used in the present study, the dynamic responses of the flexible plate wing shown in Fig. 5 are calculated and compared with the results obtained by using the finite element solver ANSYS. The purpose of the study is to find out how many mode shapes are required for accurate representation of the structural motion under dynamic force.

The plate wing has the same outline as the AGARD wing 445.6, and its first mode natural vibration frequency is nearly the same as the corresponding one of the AGARD wing 445.6. The thickness of the plate is 0.3", the root chord is 21.96", the tip chord is 14.49", and the spanwise length is 30". The plate wing consists of 80 elements and 861 node points on each side of the wing. The plate wing is held fixed on the root.

A time-dependent force is exerted at node point 510, which is located at the mid-point of the wing tip. The three components of the force in the unit of pound are:

$$\begin{aligned} f_x &= 0.5 \sin(2\pi f_c t), & f_y &= 0.3 \sin(2\pi f_c t), \\ f_z &= 0.8 \sin(2\pi f_c t) \end{aligned} \quad (44)$$

where the exciting frequency f_c is equal to 10 Hz. The modal damping ratio $\zeta_j = 0.01$, the time step used is 0.0005 s. The dynamic responses at several locations are recorded. Fig. 6 shows the time histories of the responses at the node point 491 which is located almost at the center of the plate wing. The numerical predictions by the present structural solver with the first five mode shapes agree excellently with the results using ANSYS with the first five mode shapes and the full model. The three results are virtually identical.

5.3. AGARD wing 445.6 flutter

The AGARD 445.6 wing is selected to demonstrate the capability of the present solver for predicting the flutter boundary. This wing has a quarter-chord sweep angle of 45°, an aspect ratio of 1.65, a taper ratio of 0.6576, and a NACA65A004 airfoil section in the streamwise direction. The weakened wing model (Model 3) listed in [16] is chosen for this study. The geometry of the wing and its first six

mode shapes as well as the experimental flutter results are also provided in the same report [16]. The wing structure is modeled by its first five natural vibration modes in the present computation.

The simulations start with the stationary rigid body wing model. After the steady state flow field around the wing is fully developed, the rigid body wing is switched to the flexible wing model. As a small imposed perturbation, the first mode displacement of the structural motion is set into sinusoidal motion for one cycle with the maximum amplitude of 0.0005–0.001 and the first mode frequency of the wing. Then the wing is allowed to deflect in response to the dynamic force load. Within each physical time step, the solution usually converges in 50–100 iterations.

In Figs. 7–9, the computed time histories of the generalized displacements of the AGARD wing 445.6 at $M_\infty = 0.96$ are plotted for three different V^* . In these figures, from $V^* = 0.28$ to $V^* = 0.315$, the plots correspond to the computed damped, neutral, and diverging responses, respectively. When the value of V^* is smaller than the critical value on the flutter boundary, the amplitudes of all modes decrease in time corresponding to the damped response as shown in Fig. 7. Once the value of V^* coincides with or is close to the critical value, the neutral response appears as shown in Fig. 8. When the value of V^* is above the neutral stability point, the amplitudes of first five modes grow rapidly, a diverging response is hence reached as shown in Fig. 9. At $M_\infty = 0.96$, the location of the predicted flutter boundary is about 0.29 which is consistent with the experimental value of 0.3076 provided by Ref. [16].

For a given Mach number, several runs with different V^* are needed to determine the location of the flutter bound-

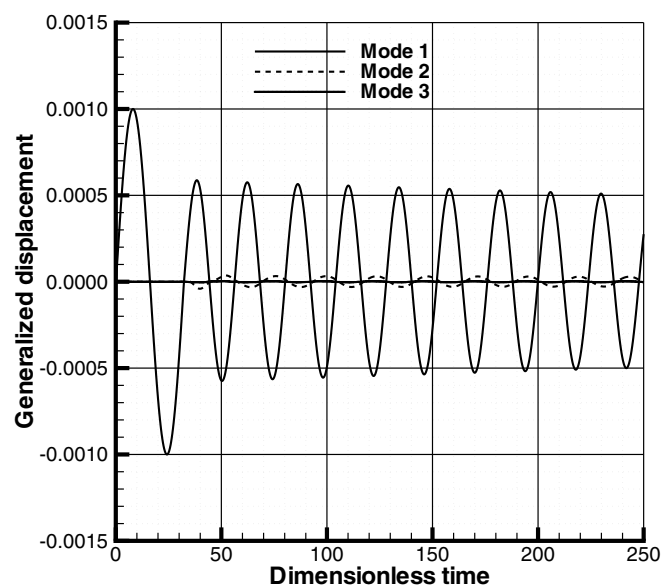


Fig. 7. Time histories of the generalized displacements of first three modes for $M_\infty = 0.96$ and $V^* = 0.28$ – damped response.

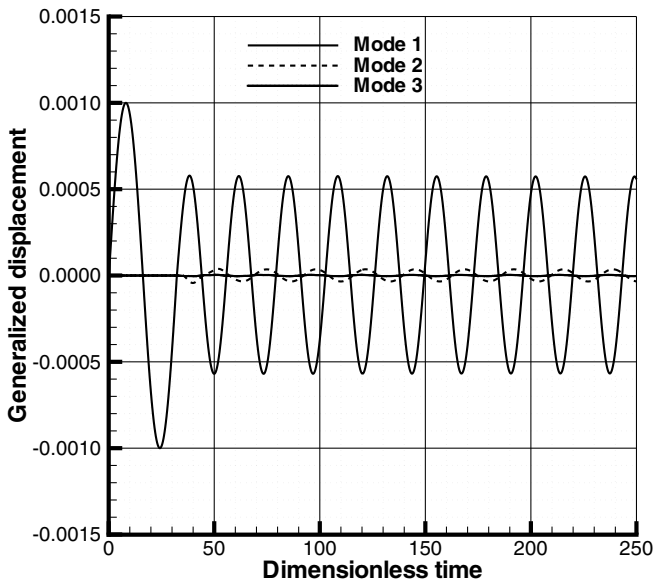


Fig. 8. Time histories of the generalized displacements of first three modes for $M_\infty = 0.96$ and $V^* = 0.29$ – neutrally stable response.

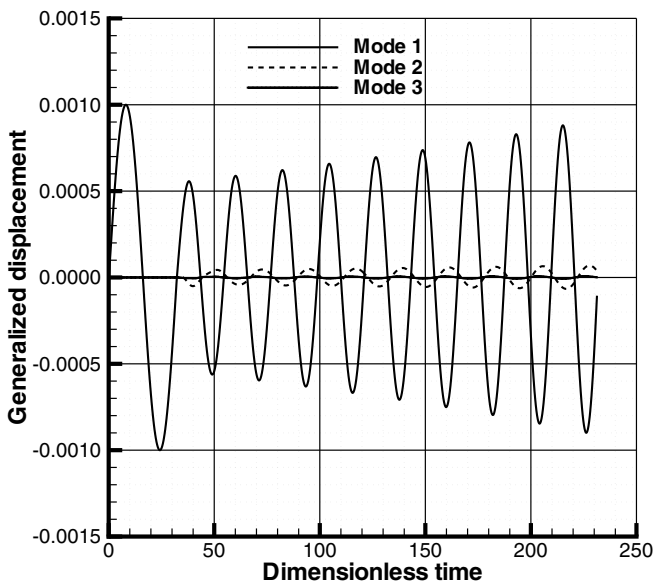


Fig. 9. Time histories of the generalized displacements of first three modes for $M_\infty = 0.96$ and $V^* = 0.315$ – diverging response.

ary using the bisection method. When V^* is varied in the computations, the free-stream Reynolds number is changed accordingly since U_∞ is varied. Strictly speaking, the free-stream Reynolds number needs to be updated and the initial steady-state flow field with actual Reynolds number should be re-generated for each run. In the present simulation, the initial flow field and the Reynolds number remain unchanged when V^* is varied. The effect on the final solution due to a small variation in the free-stream Reynolds number is negligible as examined in our numerical experiments.

Figs. 10–12 show the wing surface pressure contours at three different instants: the wing tip at uppermost, neutral and lowermost positions respectively at $M_\infty = 0.96$ and $V^* = 0.29$.

The comparison of computed flutter boundary and experimental data for AGARD Wing 445.6 is illustrated in Fig. 13. Overall, the computed results are in good agreement with the experimental data. The “sonic dip” near Mach = 1.0 measured in the experiment is very well captured by the computation. The largest discrepancy between computed and experimental results is at $M_\infty = 1.171$,

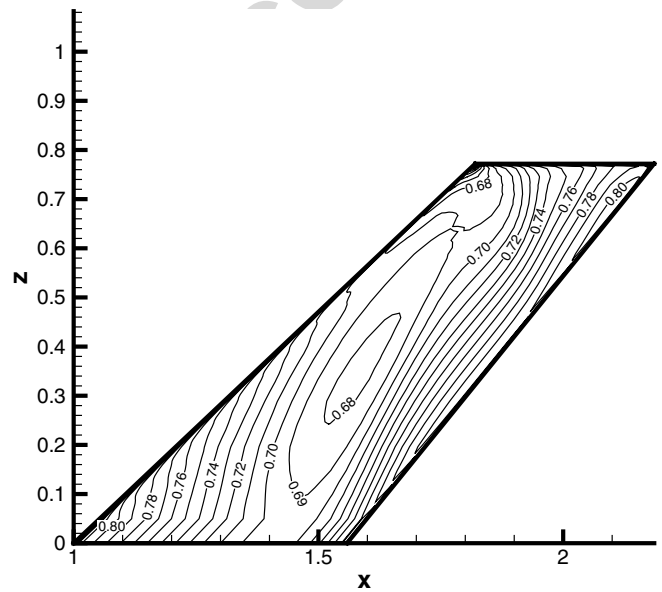


Fig. 10. Pressure distribution on the wing's surface when the tip is located at the uppermost position: $M_\infty = 0.96$ and $V^* = 0.29$.

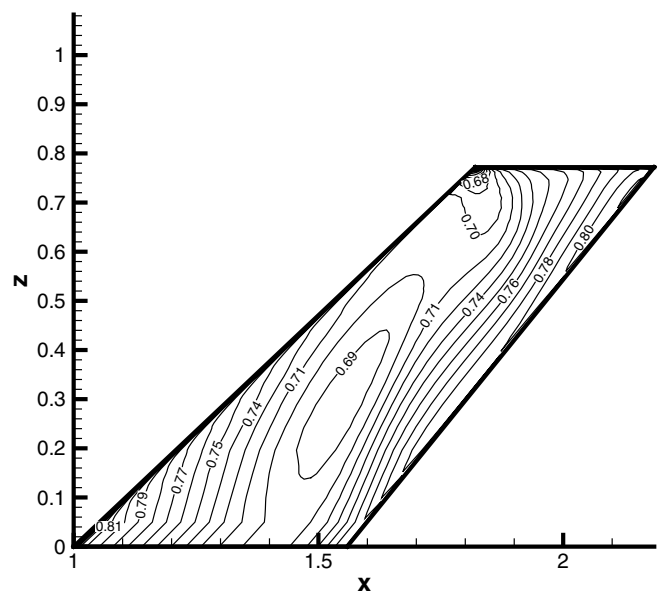


Fig. 11. Pressure distribution on the wing's surface when the tip is located at the neutral position: $M_\infty = 0.96$ and $V^* = 0.29$.

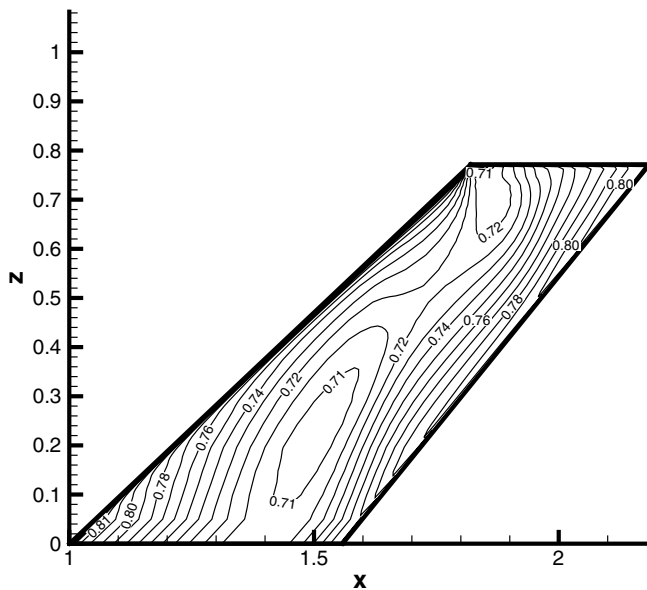


Fig. 12. Pressure distribution on the wing's surface when the tip is located at the lowermost position: $M_\infty = 0.96$ and $V^* = 0.29$.

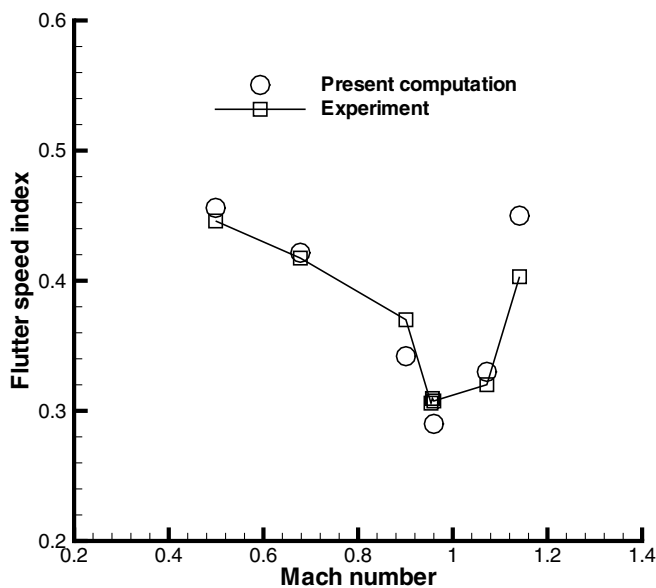


Fig. 13. Comparison of computed results and experimental data for AGARD Wing 445.6.

which is previously noted by other researchers [2,18]. It may be due to the inadequacy of the turbulent modeling to capture the shock/wave boundary layer interaction at high Mach numbers with stronger shock waves, or may be due to the inaccurate measurement in the experiment as suspected by some researchers.

6. Conclusion

A numerical methodology with fully coupled fluid-structural interaction for predicating 3-D transonic wing

flutter has been developed. A dual-time step implicit unfactored Gauss-Seidel iteration with the Roe scheme are employed in the flow solver. A modal approach structure solver is used to simulate the wing's response. An efficient mesh-deformation strategy based on an algebraic method is developed and is shown to be accurate and robust. The flow and structure solvers are fully coupled via successive iterations within each physical time step.

The accuracy of the modal approach has been verified by using the finite element solver ANSYS. The results indicate that the first five modes are sufficient to accurately model the wing structure in the present study.

The computed flutter boundary of AGARD wing 445.6 for free stream Mach numbers ranging from 0.499 to 1.141 compares well with the experimental data except for $M_\infty = 1.171$, where the flutter boundary is over-predicted. The sonic dip is very well captured.

Acknowledgement

This work is supported by AFOSR Grant F49620-03-1-0253 monitored by Dr. Fariba Fahroo.

References

- [1] Melville RB, Morton SA. Fully implicit aeroelasticity on overset grid systems. AIAA Paper-98-0521; 1998.
- [2] Lee-Rausch E, Batina J. Calculation of AGARD wing 445.6 flutter using Navier–Stokes aerodynamics. AIAA Paper 93-3476; 1993.
- [3] Lee-Rausch E, Batina J. Wing flutter computations using an aerodynamics model based on the Navier–Stokes equations. J Aircraft 1996;33:1139–47.
- [4] Morton SA, Melville RB, Visbal MR. Accuracy and coupling issues of aeroelastic Navier–Stokes solutions on deforming meshes. AIAA Paper-97-1085; 1997.
- [5] Melville RB, Morton SA, Rizzetta DP. Implementation of a fully-implicit, aeroelastic Navier–Stokes solver. AIAA Paper-97-2039; 1997.
- [6] Gordnier RE, Melville RB. Transonic flutter simulations using an implicit aeroelastic solver. J Aircraft 2000;37:872–9. September–October.
- [7] Liu F, Cai J, Zhu Y, Wong A, Tsai H. Calculation of wing flutter by a coupled CFD-CSD method. AIAA-2000-0907; 2000.
- [8] Doi H, Alonso J. Fluid/structure coupled aeroelastic computations for transonic flows in turbomachinery. ASME Turbo Expo 2002, GT-2002-30313; 2002.
- [9] Chen X-Y, Zha G-C, Hu Z-J. Numerical simulation of flow induced vibration based on fully coupled-structural interactions. AIAA Paper 2004-2240, June 28–July 1; 2004.
- [10] Chen X, Zha G-C. Fully coupled fluid-structural interactions using an efficient high solution upwind scheme. J Fluid Struct 2005;20: 1105–25.
- [11] Baldwin B, Lomax H. Thin-layer approximation and algebraic model for separated turbulent flows. AIAA Paper 78-257; 1978.
- [12] Jameson A. Time dependent calculations using multigrid with application to unsteady flows past airfoils and wings. AIAA Paper 91-1596; 1991.
- [13] Roe P. Approximate Riemann solvers, parameter vectors, and difference schemes. J Comput Phys 1981;43:357–72.
- [14] Van Leer B. Towards the ultimate conservative difference scheme, III. J Comput Phys 1977;23:263–75.

- [15] Thomas P, Lombard C. Geometric conservation law and its application to flow computations on moving grids. *AIAA J* 1979;17:1030–7.
- [16] Yates Jr E. Agard standard aeroelastic configurations for dynamic response I. –Wing 445.6. Tech. Rep. AGARD Report No.765, AGARD, September 1985.
- [17] Schmitt V, Charpin F. Pressure distributions on the ONERA-m6-wing at transonic Mach numbers. Tech. Rep. AGARD AR 138, AGARD, May 1979.
- [18] Liu F, Zhu Y, Tsai H, Wong A. Calculation of wing flutter by a coupled fluid–structure method. *J Aircraft* 2001;38:334–42.

Author's personal copy